Hybrid piezoelectric-inductive flow energy harvesting and dimensionless electroaeroelastic analysis for scaling

J. A. C. Dias,[1] C. De Marqui, Jr.,[1] and A. Erturk[2,a]

[1]*Department of Aeronautical Engineering, Engineering School of São Carlos, University of São Paulo, São Carlos, SP 13566-590, Brazil*
[2]*G. W. Woodruff School of Mechanical Engineering, Georgia Institute of Technology, Atlanta, Georgia 30332-0405, USA*

Piezoelectric and electromagnetic transduction techniques have peculiar advantages to leverage in the growing field of flow energy harvesting from aeroelastic vibrations. This letter presents the concept of hybrid piezoelectric-inductive power generation with electroaeroelastic modeling and simulations. Dimensionless analysis of the coupled system dynamics is indispensable to proper geometric scaling and optimization of aeroelastic energy harvesters. The governing electroaeroelastic equations are given in dimensionless form, and the effects of aeroelastic and electrical properties are investigated in detail toward understanding the dependence of the cut-in speed (flutter speed) and the maximum power output of the harvester on the system parameters. © 2013 American Institute of Physics. [http://dx.doi.org/10.1063/1.4789433]

The research goal in aeroelastic energy harvesting is to enable geometrically scalable and low-profile flow energy harvesters to power small electronic components for applications ranging from health monitoring in aircraft structures to wireless sensors located in high wind areas. The combination of aeroelastic vibrations with an appropriate transduction mechanism for transforming wind energy into low-power electricity has received growing attention in the energy harvesting literature. The use of bluff-body based and airfoil-based configurations are two convenient ways to create persistent oscillations for flow energy harvesting.

The first use of a piezoelectric interface in flow energy harvesting appears to be the bluff body–polyvinylidene fluoride (PVDF) membrane configuration tested under water by Allen and Smits.[1] The von Kármán vortex street formed behind the bluff body excites the piezoelectric PVDF to extract electricity from flow-induced vibrations through the direct piezoelectric effect. For the piezoaeroelastic problem of energy harvesting from airflow excitation of a cantilevered plate with embedded piezoceramics, De Marqui et al.[2,3] presented finite-element models based on the vortex-lattice method[2] and the doublet-lattice method[3] of aeroelasticity.[4] Time-domain simulations[2] were given for a cantilevered plate with embedded piezoceramics for various airflow speeds below the linear flutter speed and at the flutter boundary. Frequency-domain simulations[3] considering resistive and resistive-inductive circuits were also presented focusing on the linear response at the flutter boundary. Bryant and Garcia[5] studied the aeroelastic energy harvesting problem for a typical section by using the finite state theory of Peters et al.[6] while Erturk et al.[7] presented an experimentally validated lumped-parameter model for a wing-section (airfoil) with piezoceramics attached onto plunge stiffness members using Theodorsen's unsteady aerodynamic model.[8] Piezoelectric power generation at the flutter boundary, including the minor shift in the linear flutter speed, has also been discussed.[7] More recently the nonlinear version of the same setup (with a free play in the pitch degree-of-freedom) has been investigated to increase the operating envelope of the aeroelastic energy harvester.[9] In particular, hardening cubic nonlinearity and free play are combined to keep the oscillation amplitudes at an acceptable level while reducing the cut-in speed.

As an alternative to airfoil-based and cantilevered wing-based configurations, St. Clair et al.[10] presented a design that uses a piezoelectric beam embedded within a cavity under airflow. Vortex-induced oscillations of piezoelectric cantilevers located behind bluff bodies were investigated by Pobering et al.[11] and Akaydin et al.[12] through experiments and numerical simulations. Giacomello and Porfiri[13] investigated underwater flapping of an ionic polymer-metal composite (IPMC) flag. More recently Peterson and Porfiri[14] studied the energy extraction mechanism from a vortex ring using an IPMC cantilever. Underwater base excitation of piezoelectric[15] and IPMC[16] cantilevers has also been investigated for low-power electricity generation.

An extensive analysis of the energy harvesting potential for a foil-damper system was presented by Peng and Zhu[17] using a Navier-Stokes model without focusing on a specific transduction mechanism. Akcabay and Young[18] investigated the energy harvesting potential of flexible beams in viscous flow along with the effects of system parameters. Tang et al.[19] presented a rigorous analysis of the energy transfer from the fluid to the structure for self-excited vibrations due to axial flow over a cantilever. Piezoelectric energy harvesting from limit-cycle oscillations under axial flow over a cantilever beam has also been discussed by Dunnmon et al.[20] recently. Kwon[21] considered a T-shaped cantilever beam that causes vortex street formation over the cantilever in response to axial flow. Kwuimy et al.[22] employed a bistable energy harvester[23] for turbulent wind energy harvesting. Recent efforts have also employed electromagnetic induction for converting aeroelastic vibrations into electricity through flutter wake galloping[24] and bluff body-based oscillations.[25]

a)Author to whom correspondence should be addressed. Electronic mail: alper.erturk@me.gatech.edu.
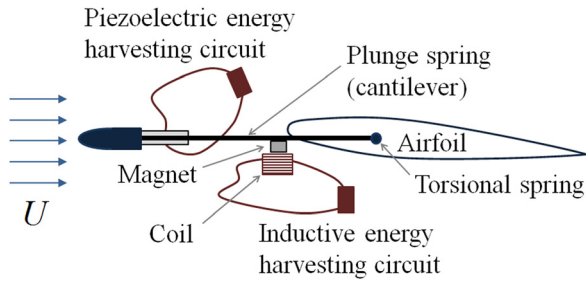
FIG. 1. Physical schematic of a hybrid piezoelectric-inductive aeroelastic energy harvester based on a 2-DOF aeroelastic section.

Piezoelectric transduction is very convenient to employ for extracting energy from structural vibrations (e.g., from the strain fluctuations of a heaving plunge cantilever) by means of attaching piezoceramic patches while electromagnetic induction is useful for exploiting relative motions (e.g., at the tip of the plunge cantilever relative to the ground). Combination of these transduction mechanisms within a single hybrid flow energy harvester can improve the power density while employing the same simple platform (Fig. 1). Moreover, dimensionless analysis of the electroaeroelastic behavior with changing electrical and aeroelastic parameters is indispensable to scaling and optimization of electroaeroelastic energy harvesters toward reducing the cut-in speed and maximizing the power output. To this end, in the present work, an airfoil-based aeroelastic energy harvester that simultaneously exploits piezoelectric transduction and electromagnetic induction is analyzed based on fully coupled electroaeroelastic modeling. As shown in Fig. 1, both forms of electromechanical coupling are introduced to the plunge degree of freedom (DOF). The interaction between total simultaneous power generation (from piezoelectric transduction and electromagnetic induction) and the electroaeroelastic behavior of the typical section is investigated in the presence of two separate electrical loads. Dimensionless electroaeroelastic equations are obtained to study the effects of certain parameters and geometric scaling of the hybrid piezoelectric-inductive energy harvester concept introduced herein.

Figure 2 shows the system parameters and variables in a hybrid piezoelectric-inductive aeroelastic energy harvester.
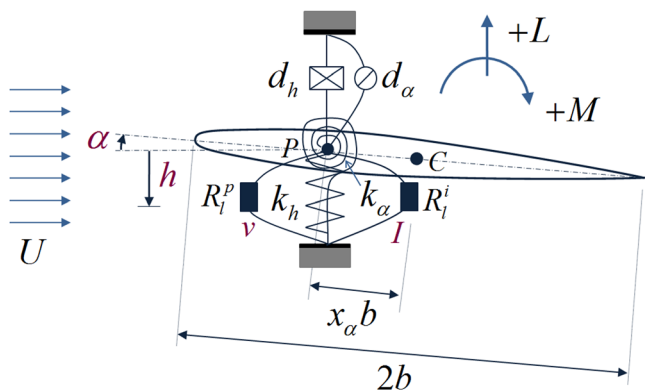

FIG. 2. Electroaeroelastic system parameters and variables in a hybrid piezoelectric-inductive aeroelastic energy harvester based on a 2-DOF aeroelastic section depicting four components of the response: plunge displacement (h), angular pitch displacement (α), piezoelectric voltage (v) across the load R_l^p, and induced current (I) flowing to the load R_l^i.

The plunge and pitch displacement variables are denoted by h and α, respectively. The plunge displacement is measured at the elastic axis (positive downward), and the pitch angle is measured about the elastic axis (positive clockwise). In addition, b is the semichord of the airfoil section, x_α is the dimensionless chord-wise offset of the elastic axis from the centroid (C), k_h is the stiffness per length (in the span direction) in the plunge DOF, k_α is the stiffness per length in the pitch DOF, d_h is the damping coefficient per length in the plunge DOF, d_α is the damping coefficient per length in the pitch DOF, and U is the airflow speed.

The electroaeroelastically coupled equations governing the dynamics of the hybrid piezoelectric-inductive flow energy harvester shown in Fig. 2 are

$$(m + m_e)\ddot{h} + mbx_\alpha\ddot{\alpha} + d_h\dot{h} + k_h h - \frac{\theta}{l}v - \frac{B_l}{l}I = -L, \quad (1)$$

$$mbx_\alpha\ddot{h} + I_\alpha\ddot{\alpha} + d_\alpha\dot{\alpha} + k_\alpha\alpha = M, \quad (2)$$

$$C_p^{eq}\dot{v} + v/R_l^p + \theta\dot{h} = 0, \quad (3)$$

$$L_c\dot{I} + (R_c + R_l^i)I + B_l\dot{h} = 0, \quad (4)$$

where m is the airfoil mass per length, m_e is the effective fixture mass (connecting the airfoil to the plunge springs) per length, I_α is the airfoil moment of inertia, L is the aerodynamic lift and M is the aerodynamic moment per length, θ is the piezoelectric coupling, B_l is the electromagnetic coupling, l is span length, C_p^{eq} is the equivalent capacitance of the piezoceramic layers, R_l^p is the load resistance in the piezoelectric energy harvesting circuit, v is the voltage across R_l^p, L_c is the internal (or inherent) coil inductance, R_c is the internal resistance of the inductor coil, R_l^i is the load resistance in the inductive energy harvesting circuit, I is the induced electric current flowing to R_l^i, and the over-dot represents differentiation with respect to time (t). The internal resistance of the piezoelectric component is neglected since it is typically much larger than the load resistance. In the aeroelastic domain, the flow is assumed to be inviscid and incompressible, and the unsteady aerodynamic loads (lift and moment terms) due to arbitrary motions are obtained from Jones' approximation[26] of Wagner's indicial function,[27] which is an approximation to the generalized Theodorsen function.[8]

Equations (1)–(4) can be written in the dimensionless form as

$$\beta\bar{h}'' + x_\alpha\bar{\alpha}'' + \zeta_h\bar{h}' + \bar{h} - \kappa\bar{v} - \chi\bar{I} = -\bar{L}, \quad (5)$$

$$x_\alpha\bar{h}'' + \bar{r}_\alpha\bar{\alpha}'' + \zeta_\alpha\bar{\alpha}' + \gamma^2\bar{r}_\alpha\bar{\alpha} = \overline{M}, \quad (6)$$

$$\eta\bar{v}' + \bar{v}/\lambda_l^p + \kappa\bar{h}' = 0, \quad (7)$$

$$\varphi\bar{I}' + \lambda_c\bar{I} + \lambda_l\bar{I} + \chi\bar{h}' = 0, \quad (8)$$

where $\beta = (m + m_e)/m$, $\bar{h} = h/b$ is the dimensionless plunge displacement, $\zeta_h = d_h/m\omega_h$ is the plunge damping factor, $\zeta_\alpha = d_\alpha/mb^2\omega_h$ is the dimensionless pitch damping factor, $\bar{r}_\alpha = r_\alpha/b$ is the dimensionless radius of gyration, $\bar{v} = v/v^*$ (where $v^* = 1$ V is the reference voltage), $\kappa = \theta v^*/lmb\omega_h^2$ is

the dimensionless piezoelectric coupling, $\eta = C_p^{eq}(v^*)^2 /mb^2 l\omega_h^2$ is the dimensionless equivalent capacitance, $\lambda_l^p = R_l^p mb^2 \omega_h^3/(v^*)^2$ is the dimensionless load resistance for the piezoelectric energy harvesting circuit, $\bar{I} = I/I^*$ (where $I^* = 1\,A$ is the reference current), $\chi = B_l I^*/lmb\omega_h^2$ is the dimensionless electromagnetic coupling, $\varphi = L_c(I^*)^2/lmb^2\omega_h^2$ is the dimensionless inductance, $\lambda_l^i = R_l^i(I^*)^2/lmb^2\omega_h^3$ is the dimensionless load resistance for the inductive energy harvesting circuit, $\lambda_c = R_c(I^*)^2/lmb^2\omega_h^3$ is the dimensionless internal resistance, $\gamma = \omega_\alpha/\omega_h$ is the frequency ratio, $\omega_h^2 = k_h/m$ is the square of the plunge natural frequency, and $\omega_\alpha^2 = k_\alpha/I_\alpha$ is the square of the pitch natural frequency. The dimensionless aerodynamic loads are $\bar{L} = L/mb\omega_h^2$ and $\bar{M} = M/mb^2\omega_h^2$. In the governing equations, the prime ($'$) denotes that the differentiation with respect to the dimensionless time $\tau = \omega_h t$.

The coupled piezoaeroelastic equations can be written in the state-space form by introducing the electromechanical coupling terms to the aeroelastic model by Edwards et al.[28] Since the dimensionless electroaeroelastic system consists of several parameters, it is necessary to investigate the effects of aeroelastic and electrical parameters on the flutter speed and power output in several cases. Since the focus is placed on the flutter boundary (to maximize the power output and reduce the linear flutter speed), the foregoing linear electroaeroelastic formulation is well-justified from the practical point of view. The authors formerly demonstrated the possibility of reducing the cut-in speed by exploiting nonlinear dynamic phenomena[9] theoretically and experimentally whereas the present work focuses on the linear system parameters.

First the effects of dimensionless radius of gyration $\bar{r}_\alpha$, frequency ratio γ, and chord-wise offset of the elastic axis from the centroid x_α on the dimensionless total electrical power as well as the dimensionless flutter speed of the hybrid piezoelectric-inductive flow energy harvester are investigated for the optimal electrical loads. Then the focus is placed on the effects of the dimensionless electrical loads and their effects on the power output and the flutter boundary. The nominal aeroelastic parameters belong to the piezoaeroelastic experimental setup used by Sousa et al.[9] ($\bar{r}_\alpha = 0.5467$, $\gamma = 0.509$, $x_\alpha = 0.25$, $\beta = 2.594$, $\zeta_h = 0.0535$, and $\zeta_\alpha = 0.1102$). The piezoelectric coupling, electromagnetic coupling, and piezoelectric capacitance have the fixed values of $\kappa = 5.9 \times 10^{-6}$, $\chi = 0.0457$, and $\eta = 3.66 \times 10^{-9}$. The simulations in the present work are performed for the dimensionless frequency ratio ranging from 0.02 to 3 times of the original value ($\gamma = 0.509$), radius of gyration ranging from 0.35 to 1.45 times the original value ($\bar{r}_\alpha = 0.5467$), and chord-wise offset of the elastic axis from the centroid ranging from 0.2 to 2 times the original value ($x_\alpha = 0.25$).

The variation of dimensionless flutter speed ($\bar{U} = U/\omega_h b$) with dimensionless radius of gyration ($\bar{r}_\alpha$) and frequency ratio (γ) is displayed in Fig. 3(a) for the optimal electrical load resistance values of each set of aeroelastic parameters in both circuits (to maximize the power output) and fixed chord-wise offset of the elastic axis from the centroid ($x_\alpha = 0.25$). The flutter speed increases with increasing $\bar{r}_\alpha$ for all values of γ. Figure 3(b) shows the variation of total dimensionless electrical power output ($\bar{P} = \bar{v}^2/\lambda_l^p + \bar{I}^2\lambda_l^i$) with $\bar{r}_\alpha$ and γ for the dimensionless flutter speed values of Fig. 3(a) (note that the $\bar{r}_\alpha$-axis is reversed for clarity). The electrical power output is minimal when the
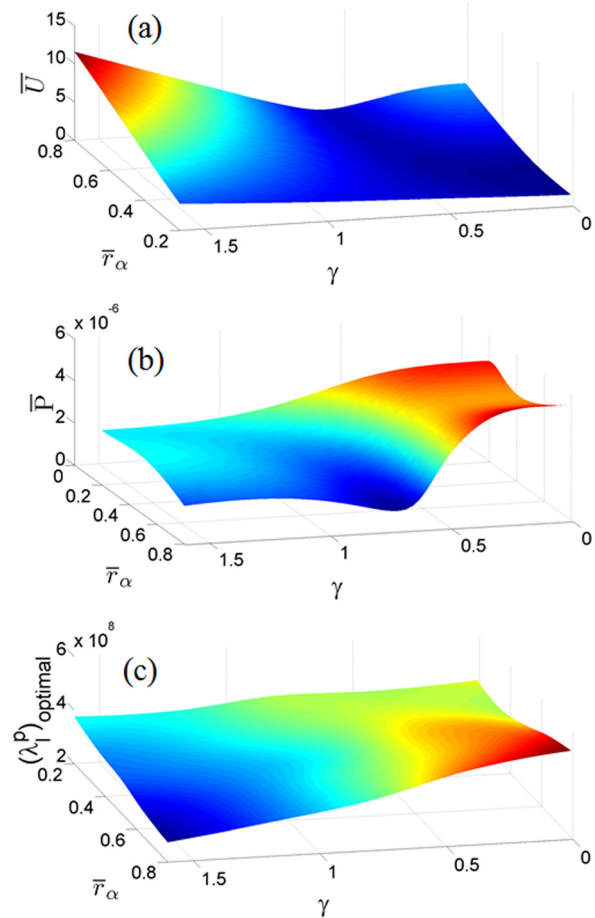

FIG. 3. Dimensionless (a) flutter speed, (b) power output, and (c) load resistance (of the piezoelectric circuit) versus dimensionless radius of gyration and frequency ratio at the flutter boundary (for a fixed chord-wise offset of the elastic axis from the centroid: $x_\alpha = 0.25$).

frequency ratio is around $\gamma = 0.7$ (which should therefore be avoided in design). Although the power output increases at higher frequency ratios above this value in the high radius of gyration regime, the flutter speed also increases. Increased flutter speed is against the practicality of the aeroelastic energy harvesting concept and should be avoided. The maximum total power output is obtained for the lowest values of radius of gyration and frequency ratio. This preferred area also corresponds to the configurations with the lowest flutter speed. In Figs. 3(a) and 3(b), the dimensionless load resistance for the inductive energy harvesting circuit that generates maximum power output remains close to the value of dimensionless internal coil resistance, $(\lambda_l^i)_{optimal} \cong \lambda_c = 0.1022$ (in agreement with the maximum power transfer theorem[26]) while the optimal electrical load of the piezoelectric energy harvesting circuit is shown in Fig. 3(c) for the $\bar{r}_\alpha$ and γ combinations shown in Figs. 3(a) and 3(b).

The dependence of dimensionless flutter speed on dimensionless chord-wise offset of the elastic axis from the centroid (x_α) and frequency ratio (γ) is displayed in Fig. 4(a) for the optimal electrical load resistance values (for each combination of aeroelastic parameters) in both circuits and fixed dimensionless radius of gyration ($\bar{r}_\alpha = 0.5467$). The flutter speed increases with decreasing x_α (reducing the inertial coupling of the DOFs) for all values of γ. Figure 4(b) shows the variation of total dimensionless electrical power
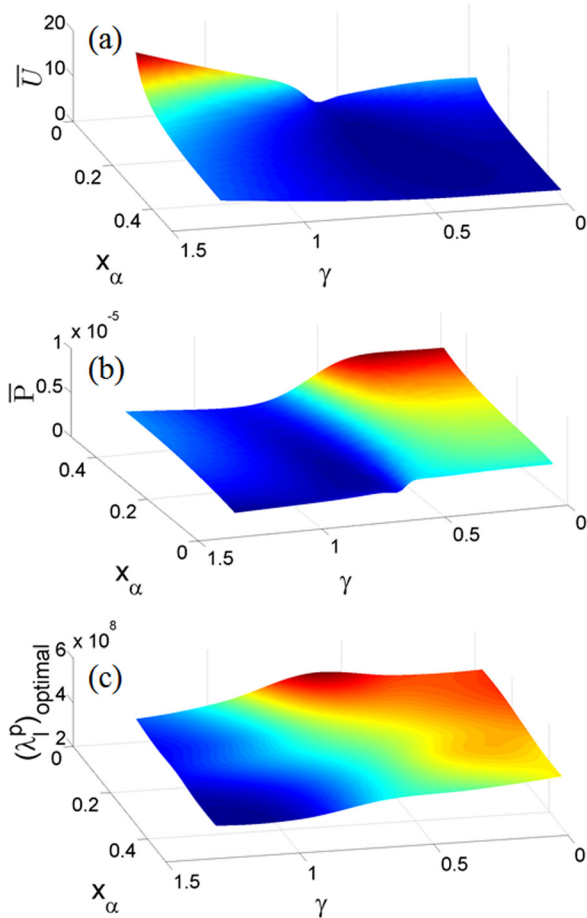
FIG. 4. Dimensionless (a) flutter speed, (b) power output, and (c) load resistance (of the piezoelectric circuit) versus dimensionless chord-wise offset of the elastic axis from the centroid and frequency ratio at the flutter boundary (for a fixed dimensionless radius of gyration: $\bar{r}_\alpha = 0.5467$).
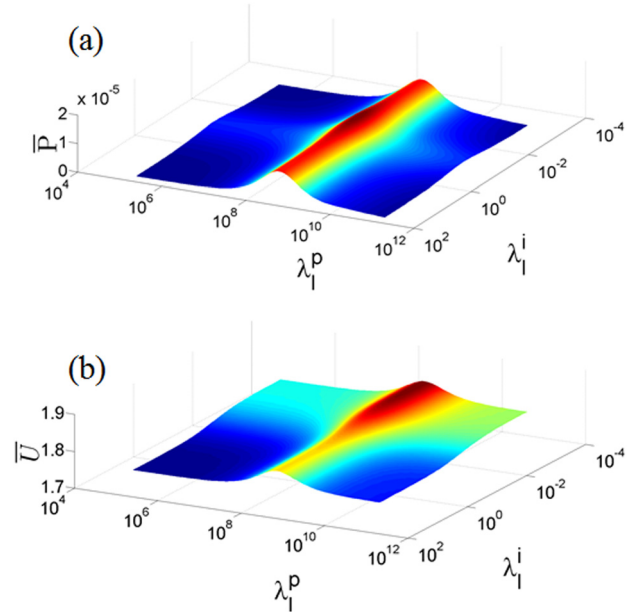

FIG. 5. Dimensionless (a) power output and (b) flutter speed versus dimensionless electrical loads of both circuits (for non-zero coil resistance in the inductive circuit: $\lambda_c = 0.1022$).

output with x_α and γ obtained at each dimensionless flutter speed of Fig. 4(a) (note that the x_α-axis is reversed for clarity). The electrical power output is minimal for the frequency ratios near $\gamma = 0.7$ and for low values of x_α (where the flutter speed is high). The maximum total power output is obtained for the lowest γ and highest x_α, and this favorable area also corresponds to low values of flutter speed (Fig. 4(a)). Once again, the optimal load resistance for the inductive energy harvesting circuit remains close to the value of dimensionless internal coil resistance $((\lambda_l^i)_{optimal} \cong \lambda_c = 0.1022)$ while the optimal electrical load of the piezoelectric energy harvesting circuit is shown in Fig. 4(c) for changing x_α and γ.

Next the effects of dimensionless resistive loads in the inductive and piezoelectric energy harvesting circuits on dimensionless electrical power as well as dimensionless flutter speed of the hybrid piezoelectric-inductive flow energy harvester are investigated. The ranges of resistive loads in the piezoelectric and inductive circuits cover the interval of short-circuit to open-circuit conditions for each circuit. A coil with an inductance of 428 mH (yielding $\varphi = 0.0130$) and internal resistance of 175 Ω (yielding the aforementioned $\lambda_c = 0.1022$) is assumed for the inductive circuit. The remaining system parameters are assumed to take their nominal values mentioned previously.

The interaction between electrical power generation (from piezoelectric transduction and electromagnetic induction) and electroaeroelastic behavior at the flutter boundary is shown in Fig. 5 for broad ranges of separate resistive loads connected to the respective transduction interfaces (see Figs. 1 and 2). The variation of the total dimensionless power output $(\bar{P})$ with dimensionless load resistance values is given in Fig. 5(a). The maximum power output is observed for the combination of the optimal resistive load values of each external circuit. The optimal load of the inductive circuit is again around the coil resistance $(\lambda_c = 0.1022)$ in agreement with the maximum power transfer theorem.[29] The variation of dimensionless flutter speed $(\bar{U})$ with dimensionless resistive loads of the piezoelectric and inductive energy harvesting circuits is presented in Fig. 5(b). The presence of an optimal load resistance for the piezoelectric circuit that gives the maximum flutter speed is observed for all values of load resistance of the inductive circuit. The flutter speed decreases with increasing load resistance of the inductive circuit for any value of load resistance of the piezoelectric circuit. The fact that the optimal load resistance of the maximum power output in the inductive circuit does not correspond to that of the maximum flutter speed might seem to be counterintuitive. However, it is simply a consequence of the realistic non-zero internal coil resistance assumption in the presence of non-zero coil inductance. It can easily be shown even for vibration-based electromagnetic energy harvesters (Amirtharajah and Chandrakasan[30] and Elvin and Elvin[31]) that the short-circuit stiffness is larger than the open-circuit stiffness due to electromagnetic coupling in the presence of non-zero coil inductance. The variations of the flutter speed and power output dramatically depend on the presence of internal coil resistance in the inductive energy harvesting circuit. The zero coil resistance case is addressed next for demonstration.

The variations of the total dimensionless power output and flutter speed with dimensionless resistive loads are presented in
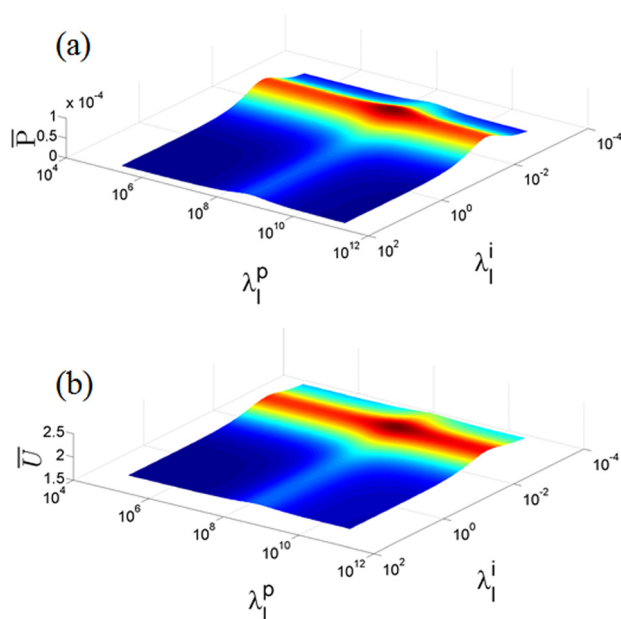
FIG. 6. Dimensionless (a) power output and (b) flutter speed versus dimensionless electrical loads of both circuits (for zero coil resistance in the inductive circuit: $\lambda_c = 0$).

Figs. 6(a) and 6(b), respectively, for zero coil resistance ($\lambda_c = 0$). Similar to the previous case (non-zero coil resistance), an optimal load resistance for the piezoelectric energy harvesting circuit that gives the maximum flutter speed is observed for all values of load resistance of the inductive energy harvesting circuit. However, in the present case of $\lambda_c = 0$, the presence of an optimal load resistance for the inductive circuit that gives the maximum flutter speed is also observed for all values of load resistance of the piezoelectric circuit. Furthermore the amount of dimensionless power output from electromagnetic induction is dramatically boosted in the absence of internal coil resistance.

An airfoil-based hybrid flow energy harvester that simultaneously exploits piezoelectric transduction and electromagnetic induction has been introduced and analyzed based on fully coupled electroaeroelastic modeling. Dimensionless analysis of the electroaeroelastic behavior has been presented for proper scaling and optimization of hybrid piezoelectric-inductive energy harvesters toward reducing the cut-in speed and maximizing the power output. The effects of several dimensionless system parameters (radius of gyration, chord-wise offset of the elastic axis from the centroid, frequency ratio, load resistances, and internal coil resistance) on the dimensionless electrical power as well as the dimensionless cut-in speed have been investigated. It is concluded that

reducing the dimensionless radius of gyration ($\bar{r}_\alpha$) and frequency ratio (γ, specifically well below $\gamma = 0.7$), while increasing the dimensionless chord-wise offset of the elastic axis from the centroid (x_α) favorably increases the power output and reduces the cut-in speed. These results and favorable parameter regions can be used for design and fabrication of optimal airfoil-based[5,7] piezoelectric-inductive flow energy harvesters for the maximum electrical power output at reasonable airflow speeds.

[1]J. J. Allen and A. J. Smits, J. Fluids Struct. **15**, 629–640 (2001).
[2]C. De Marqui, Jr., A. Erturk, and D. J. Inman, J. Intell. Mater. Syst. Struct. **21**, 983–993 (2010).
[3]C. De Marqui, Jr., W. G. R. Vieira, A. Erturk, and D. J. Inman, ASME J. Vibr. Acoust. **133**, 011003 (2010).
[4]R. L. Bisplinghoff and H. Ashley, *Principles of Aeroelasticity* (John Wiley & Sons, New York, 1962).
[5]M. Bryant and E. Garcia, ASME J. Vibr. Acoust. **133**, 011010 (2011).
[6]D. A. Peters, S. Karunamoorthy, and W. M. Cao, J. Aircraft **32**, 313–322 (1995).
[7]A. Erturk, W. G. R. Vieira, C. De Marqui, Jr., and D. J. Inman, Appl. Phys. Lett. **96**, 184103 (2010).
[8]T. Theodorsen, NACA Technical Report No. 496, 1935.
[9]V. C. Sousa, M. Anicézio, C. De Marqui, Jr., and A. Erturk, Smart Mater. Struct. **20**, 094007 (2011).
[10]D. St. Clair, A. Bibo, V. R. Sennakesavababu, M. F. Daqaq, and G. Li, Appl. Phys. Lett. **96**, 144103 (2010).
[11]S. Pobering, S. Ebermeyer, and N. Schwesinger, Proc. SPIE **7288**, 728807 (2009).
[12]H. D. Akaydin, N. Elvin, and Y. Andreopoulos, Exp. Fluids **49**, 291–304 (2010).
[13]A. Giacomello and M. Porfiri, J. Appl. Phys. **109**, 084903 (2011).
[14]S. Peterson and M. Porfiri, Appl. Phys. Lett. **100**, 114102 (2012).
[15]A. Erturk and G. Delporte, Smart Mater. Struct. **20**, 125013 (2011).
[16]M. Aureli *et al.*, Smart Mater. Struct. **19**, 015003 (2010).
[17]Z. Peng and Q. Zhu, Phys. Fluids **21**, 123602 (2009).
[18]D. T. Akcabay and Y. L. Young, Phys. Fluids **24**, 054106 (2012).
[19]L. Tang, M. Paidoussis, and J. Jiang, J. Sound Vib. **326**, 263–276 (2009).
[20]J. A. Dunnmon, S. C. Stanton, B. P. Mann, and E. H. Dowell, J. Fluids Struct. **27**, 1182–1198 (2011).
[21]S. D. Kwon, Appl. Phys. Lett. **77**, 164102 (2010).
[22]C. A. Kwuimy, G. Litak, M. Borowiec, and C. Nataraj, Appl. Phys. Lett. **100**, 024103 (2012).
[23]A. Erturk, J. Hoffmann, and D. J. Inman, Appl. Phys. Lett. **94**, 254102 (2009).
[24]H. J. Jung and S. W. Lee, Smart Mater. Struct. **20**, 055022 (2011).
[25]D. Zhu, S. Beeby, J. Tudor, N. White, and N. Harris, in Proceedings of IEEE on Sensors, Kona, HI, 1–4 November 2010, pp. 1415–1418.
[26]R. T. Jones, NACA Technical Report No. 667, 1938.
[27]H. Wagner, Z. Angew. Math. Mech. **5**, 17–322 (1925).
[28]J. W. Edwards, H. Ashley, and J. V. Breakwell, AIAA J. **17**, 365–374 (1979).
[29]A. Agarwal and J. Lang, *Foundations of Digital and Analog Electronic Circuits* (Morgan Kaufmann, San Francisco, 2005).
[30]R. Amirtharajah and A. P. Chandrakasan, IEEE J. Solid-State Circuits **33**, 687–695 (1998).
[31]N. Elvin and A. Elvin, J. Sound Vib. **330**, 2314–2324 (2011).